

AO11 - Instrument to sample and return airborne particles from an unmanned aerial vehicle

Supervisors — Drs. D. Peters, R. Grainger & A. Povey

Abstract

This project enhanced the technical design of a low-cost, handheld, operational electrostatic precipitator (ESP) that has been built for use in an unmanned aerial vehicle (UAV) to collect *in situ* samples of aerosol particles from the troposphere and analyse their properties. Collected samples of laboratory-generated aerosols were imaged using both optical and scanning electron microscopes. The particle concentration and size distribution of a black carbon (soot) aerosol sample was calculated and compared to expected results. The accuracy of this analysis technique was scrutinised. A qualitative analysis of optical deposition was achieved for soot and sea salt aerosols. Operating code for the remote activation of the instrument during flight was improved. A preliminary design for an ESP inlet was investigated, along with what factors contribute to its properties for optimum sampling of atmospheric aerosols.

1 Introduction

In recent years, the need for a better understanding of the physical properties of aerosols has increased. Aerosols are suspensions of particles in gas [1]. They have major impacts on several aspects of life, from climatology to air traffic safety. Being able to measure aerosol properties directly, such as particle shape and size, and the distribution thereof, is highly desirable for understanding changes in the climate and the Earth's radiation budget [2]. There are several local sources of aerosols (e.g. volcanic eruptions, crashing waves) and they evolve on rapid timescales [3]. Aerosols do not last long in the atmosphere and spread inhomogeneously. These effects would be better quantified if more were known about atmospheric aerosols so that we can provide input to Mie scattering¹ algorithms and include information on the properties of newly produced aerosols.

Aerosols are one of the most uncertain aspect of understanding climate change and it is important to study them in as much detail as possible [2]. Currently, the effect of aerosols is largely observed through remote measurements from satellites and ground-based instruments [1]. Measurements of properties of the atmosphere (e.g. optical depth, albedo, refractive index and absorption) by satellites give column-averaged information over the total volume of air measured. The atmosphere

within these columns varies significantly spatially and temporally. The averaged result of aerosol measurements is similar to that of thin clouds and hence is difficult to distinguish from them. [4] In order to improve satellite retrieval algorithms to identify aerosol clouds, scientists are now trying to better constrain aerosol properties on a micro-physical scale, i.e. the properties of individual particles. Exploring these fundamental properties, reducing their uncertainties and extrapolating to a statistical ensemble of many particles will help scientists to better understand the complex macroscopic properties observed, as well as the effect of aerosols on the atmosphere.

This ongoing investigation is concerned with developing a handheld instrument with which the properties of atmospheric aerosol particles can be quantified. Several accurate instruments have been designed for use on the ground (such as filter paper techniques and the scanning mobility particle sizer (SMPS) instrument) and in aircraft, but the advantage of an *in situ* handheld aerosol sampler that is small, lightweight and cost effective is that it can be used within an unmanned aerial vehicle (UAV). These remote controlled airplanes are much cheaper to produce and fly than an aircraft and therefore are expendable. As a result, the UAV's atmospheric coverage is increased to regions that are dangerous to be accessed by larger, manned aircraft. UAVs can also be flown with little preparation; in the event of new volcanic activ-

¹Theory of how electromagnetic radiation is scattered from spherical particles.

ity a UAV could be first on the scene to sample newly created aerosols. The information acquired from analysing samples is hugely beneficial when improving existing aerosol analysis techniques.

Dr. Peters and colleagues have taken these ideas to develop a handheld electrostatic precipitator (ESP) that will ultimately be used to sample atmospheric aerosols with the aid of a UAV. Hunt [5] has sourced components required for its operation. The ESP was operational before the start of this project.

This project has two main goals. Firstly, we want to quantify the validity of some analysis techniques that could be used on ESP samples. Imaging samples with a scanning electron microscope (SEM) will give us information on particle sizes and their distribution; we can compare this to accurate particle sizing data acquired from an SMPS instrument. The suitability of acquiring accurate information from analysing samples with an attenuated total reflectance (ATR) instrument will also be quantified. Secondly, steps will be taken to install the ESP within a UAV. We will look at how the instrument's inlet should be designed for optimal sampling of the atmosphere, as well as how the instrument could be activated remotely.

1.1 Background

There are several techniques used to collect samples of aerosols. Morrow and Mercer [6] first considered the concept of a point-to-plane electrostatic precipitator. Their ideas were developed further by Miller et al. [7], who experimented with a compact, handheld design of the instrument and characterised its optimal operating conditions. Dr. Peters and colleagues have built an operational ESP based on these findings.

The ESP requires a flow through the instrument that provides a continuous supply of aerosol. These particles are collected via electrostatic precipitation. This technique removes particles from the flow by producing a strong electric field between a high voltage supply on a needle i.e. the *point* in Fig. 1, and a grounded metal substrate i.e. the *plane*. A voltage in this range leads to a high density of electric field lines near the tip of the needle, resulting in corona discharge² [8] that is localised to this region. Ionised air is formed in this region and flows towards the grounded substrate. During their path towards ground, the ions deposit charge onto particles in the aerosol flow.

²A local breakdown of the dielectric medium (in this case air) which is ionised to form charged particles. A further increase in voltage would lead to arcing, i.e. dielectric breakdown, between the point and plane.

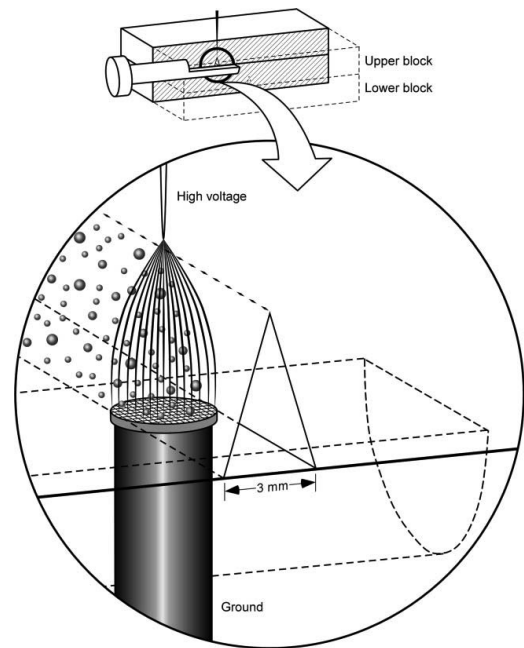


Figure 1: Diagram showing the theoretical collection of aerosol through electrostatic precipitation according to Miller et al. [7]

These newly charged larger particles also accelerate towards ground and deposit on the substrate. When the electric field is switched off, these aerosol particles stay adhered to the substrate via the van der Waals interaction.

As shown in Fig. 1, the electric field leading to particle collection is housed within a tube with triangular cross section. This shape matches the shape of the electric field well [7]. The risk of arcing between needle and ground is negated through the geometry of the field.

1.1.1 Instrument design

The aerosol collection housing was manufactured from polycarbonate, a dielectric material that is robust, lightweight and cheap to manufacture. A tungsten needle forms the high voltage point source, and it is sharpened (manually) to maximise the spread of the resulting electric field. This ensures the field lines are as homogeneous as possible on the substrate surface, whilst localising the corona discharge to the immediate region surrounding the needle. Sharpening also increases the generated ion concentration. More charge can be transferred to aerosol particles, and so the collection efficiency is optimised [7]. The substrate is formed from a cylindrical pin made of a 98% Al 2% Mg alloy that is suitable for use within a SEM instrument. This pin is polished with a glycerol diamond solution to sub-micron smoothness, so that particles should theoretically deposit homogeneously on the pin surface.

As shown in Fig. 15, there are three electrostatic precipitation regions. Hence there are three sets of

needles and pins that are placed 20 mm apart along the flow chamber. They are separated far enough such that they should act independently, so that theoretically three samples can be acquired in one test. The flow is generated with a diaphragm pump and measured with a flow sensor. More information is found in the appendix.

The operation of the ESP instrument is controlled via three Arduino boards [9] situated next to the ESP housing. The operating code was designed such that it requires human input through the software. Operating parameters such as flow rate and voltage could be varied. Commands are echoed through the serial port via a USB cable, which also provides the 5 V power supply required by the boards.

1.1.2 The UAV

The final instrument is to be installed in the Quest UAV 300 [10]. There will be limitations on the weight and size of the entire instrument. The maximum payload weight supported is 3 kg, but this has a significant effect on the flight time. Designing a handheld ESP still does not guarantee that a UAV will fly for long enough to collect a valid sample, or if the ESP components will function correctly in flight. Hence lightweight materials and technology have been sourced by Hunt [5] to ensure that the flight time is as long as possible, and that components will work within the UAV constraints.

1.2 ESP operation

The ESP components are exposed to the environment; the variable parameters (such as voltage between needle and pin, current load and flow rate) are subject to random fluctuations. It is important to quantify these fluctuations and to what extent they deviate from the commanded value, to ensure that the ESP operates as we expect it to.

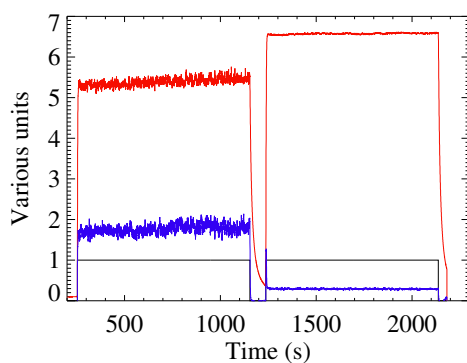


Figure 2: Measured **voltage** (kV) and **current load** (μA) of the ESP as the electric field was switched on and off.

As shown in Fig. 2, there is a significant difference in the fluctuations and magnitudes of voltage

and current load when the field is switched off and on again. This behaviour means that operation is not repeatable. Variations in the voltage could affect the concentration of ions in the corona and hence the collection efficiency. The suitable voltage range for correct electrostatic precipitation is between 5.6 and 6.8 kV, as described by Miller [7].

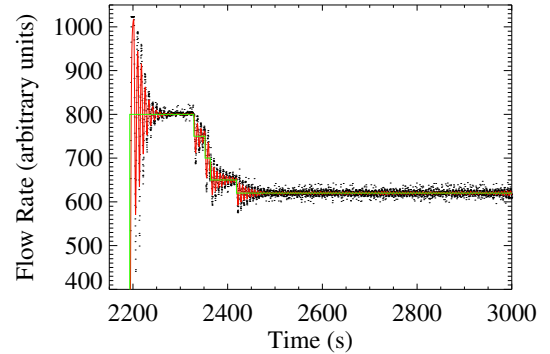


Figure 3: Variations in the measured flow rate per reading (dotted) and per **average reading** (over 0.2 s interval) compared with **commanded flow rate**.

To ensure that fluctuations are minimised and that the aerosol field is sampled evenly, the flow (generated by the diaphragm pump) should be kept as uniform as possible and at the required rate. A constant flow rate helps with predictions of how long aerosol particles should be collected for (i.e. the exposure time) to acquire a sample where the area of the pin head is fractionally covered with particles (i.e. the loading). The pump has no means of altering its operating rate to accommodate any changes in the flow. Hence a PID loop³ was incorporated by Dr. Peters and Hunt [5] into the Arduino code. The loop's effect on the expected flow rate is shown in Fig. 3. Note the overshoot after each new commanded flow that is typically associated with PID control.

2 Particle deposition analysis

One goal of this project was to quantify the properties of aerosol particles collected through ESP samples, and then compare them with what is expected. In order to understand how particles are deposited, the ESP sampled aerosols generated in controlled conditions. It was assumed that the pin loading equates linearly to the time that the electric field is on (i.e. exposure time) and that aerosol

³Proportional integral differential loops adjust the flow rate depending on the current deviation from commanded value (P), the history of deviations (I) and the current rate of change of the deviation (D).

particles follow a lognormal size distribution [11]:

$$n(r) = \frac{1}{\sigma r \sqrt{2\pi}} \exp \left[-\frac{1}{2} \left(\frac{\ln r - \ln r_g}{\sigma} \right)^2 \right], \quad (1)$$

where r is the particle radius, r_g is the mean radius and σ is the standard deviation of $\ln r$.

2.1 Black carbon aerosol

A miniCAST⁴ instrument [12] was used to generate a black carbon aerosol at the Rutherford Appleton Laboratory (RAL). The aerosol was diluted with air; decreasing the concentration of particles means that longer exposure times would be required to obtain the same loading, with the advantage that there is less chance of carbon particles coagulating along their path⁵. After dilution the aerosol flow was split, one pipe feeding into the ESP for collection and the other into a GRIMM SMPS [13] particle analyser. The SMPS contains a Condensation Particle Counter (CPC) that allows butanol to condense onto small aerosol particles, which continue to grow in radius so that they can be accurately detected and their size deduced optically via laser scattering⁶. This information is crucial for approximating the exposure times required to achieve a given loading, assuming that aerosol particles are spherical.

2.1.1 SEM regime

In this part of the project we attempt to understand the properties of individual carbon particles and their distribution as an ensemble. The SMPS instrument can accurately measure the size distribution, mean particle size and standard deviation of the carbon particles that would also be collected by the ESP. Therefore by comparing experimental and expected size distributions we can quantify how well ESP samples represent the aerosol field and the validity of our chosen analysis technique. The pin was imaged using a SEM. Images were analysed by calculating the area covered by each carbon particle and therefore the mean particle radius, assuming particles are spherical. These findings were compared to the expected size distribution and number density. The samples taken had to ensure that the majority of particles deposited did not overlap on the pin surface, which will be imaged using an SEM. Hence a low loading

⁴Propane is set alight and soot aerosol is generated by incomplete combustion of the flame. The aerosol is then mixed with nitrogen gas.

⁵We are not concerned with these larger agglomerates.

⁶Laser scattering does not work well at particle sizes below 50 nm as particle sizes are comparable to laser light wavelength, hence scattering is heavily attenuated and not all particles are detected.

($\leq 10\%$) was chosen to observe particle coverage. Exposure times ($\tau_{exposure}$) were calculated using the following equation:

$$\tau_{exposure} = \frac{r_{pin}^2}{r_m^2 \times n \times Q} \times \left[\frac{\text{Loading (\%)}}{100} \right], \quad (2)$$

where n = number density, Q = flow rate (55 cc min^{-1}), r_m is the mean radius of particles measured by the SMPS and r_{pin} is the pin radius (3 mm). A collection efficiency of 100% was assumed when calculating these exposure times. Fig. 4 shows that there are two clear regimes of

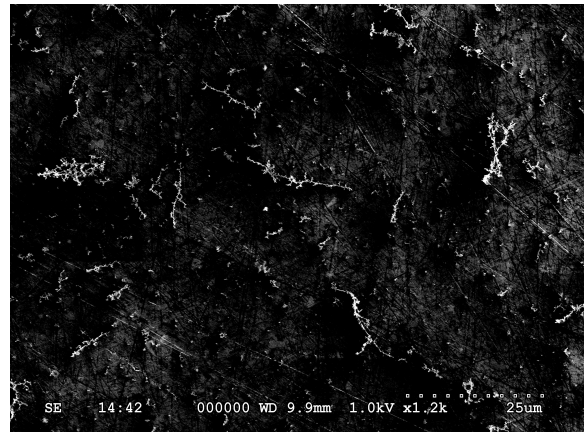


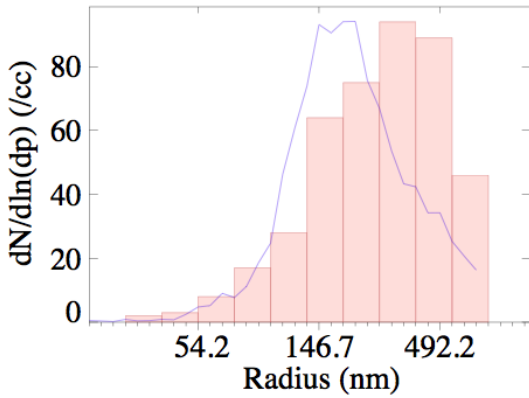
Figure 4: High contrast SEM image of deposited soot particles (white) against the pin alloy background (black) of a sample with 0.89% loading.

soot particle sizes (the sub-micron level dots and several micron structures). This implies that there were two very different size distributions of carbon particles generated by the miniCAST flame. The larger particles should have been observed by the APS⁷ instrument but only noise was observed. This leads to uncertainty in the origin of these structures. As we are not concerned with particles with radii larger than $\sim 1 \mu\text{m}$, images were taken selectively of regions covered with sub-micron particles. A loading of 0.89% worked very well in analysis as very few particles overlapped on the pin surface. In contrast, most particles in a 8.9% loaded pin overlapped due to the non-spherical particle shape. This is not beneficial for image analysis; hence only the lower loading pin was imaged.

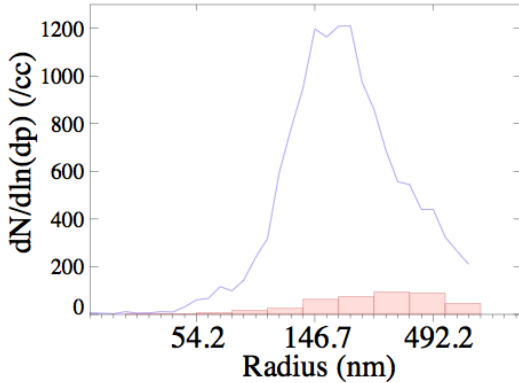
2.1.2 SEM image analysis

Images acquired from the SEM were processed using ImageJ software [14]. Magnified images similar to Fig. 4 were taken and the background was eliminated by adjusting the pixel colour threshold, before noise and anomalies were removed. The area covered by all the particles per image was calculated, along with the areas covered by individual

⁷Aerodynamic particle sizer - an instrument based on time of flight that measures particle sizes larger than $\sim 1 \mu\text{m}$.



(a) Peak normalised comparison.



(b) Number normalised comparison.

Figure 5: SMPS size distribution (line) normalised to the experimental bar data. $dN/d\ln(dp)$ is the number concentration of particles in bins of particle sizes between $\ln(dp)$ and $\ln(dp) + d\ln(dp)$, where p is the particle radius.

particles. 27 of the images acquired were suitable for analysis, and the average coverage of the pin was calculated as 2.15%. The radii of particles deposited were calculated and the mean radius was found to be 185 nm. The predicted mean radius was 113 nm. Using Equ. 2 an experimental estimation of particle concentration was calculated as $102\,795.6\text{ cc}^{-1}$. The SMPS prediction for concentration was $22\,380.6\text{ cc}^{-1}$.

Fig. 5 shows comparisons of the experimental size distribution and predicted results. The distribution shape is similar to what is predicted but only when compared on a peak normalised scale. There are several reasons to the discrepancies between expected and predicted results in Fig. 5b.

As stated in Miller et al. [5, 7], the velocity of particles within the electric field depends on each particle's electrical mobility and is given by:

$$\vec{V} = \vec{V}_{flow} + \vec{V}_{E-field} \equiv \vec{V}_{flow} + \frac{C_c ne \vec{E}}{3\pi\eta d}, \quad (3)$$

where d gives the particle diameter, η gives the dynamic viscosity of air, ne is the total charge on the aerosol particle and C_c is the Cunningham slip correction, which is required to calculate drag

forces on particles for high Knudsen number⁸ Kn (as we are considering a flow in the regime between continuum fluid and free molecular flow). Hunt derives empirical values for $\vec{v}_{E-field}$ for a range of particle sizes. For sub-micron diameters, larger particles have a lower velocity induced by the electric field (300nm diameter corresponds $\vec{V}_{E-field} = 0.40\text{ ms}^{-1}$) and smaller particles have a larger velocity (10nm diameter results in $\vec{V}_{E-field} = 2.56\text{ ms}^{-1}$). If all particles travel at the same initial velocity due to the 55 cc min^{-1} rate (i.e. $\vec{V}_{flow} = 0.122\text{ ms}^{-1}$), then it is clear that the angle⁹ θ that particles make to the flow axis will depend on their size; varying particle trajectories would result in anisotropic deposition on the pin surface. Very specific pin regions were chosen for imaging instead of random pin locations, therefore a reduced distribution of particles could have been imaged, resulting (partly) in the discrepancy observed.

Errors in the pin loading estimate could be because the deposition is inhomogeneous; more particles were observed nearer the pin centre. Images were taken of well covered regions to obtain as many particles as possible for analysis. Therefore due selective imaging loading calculations might not be representative of the whole pin. This would explain why the calculated loading is higher than predicted. The SEM was difficult to focus due to three focusing parameters that had to be adjusted simultaneously. This may have led to the smaller particles not being resolved as well as larger ones and hence they would not have been counted during image processing. The lack of small particles explains why the experimental mean radius was larger than predicted. These differences in experimental loading and mean radius lead to the very different estimate for number density, when we consider Eq. 2.

Carbon particles are also not spherical, but in fact have fractal dimension. Their shape is anisotropic and therefore when samples are imaged, the area covered by each particle greatly depends on its orientation upon deposition. This also brings into question how one converts the size distributions calculated experimentally (bearing in mind fractal structure) to compare with the CPC measurements.

As stated in Miller et al. [7], collection efficiency varies with particle size; it is not not always 100%. This will affect the deposited size distribution.

⁸The ratio of fluid mean free path to the length scale of the particle in question.

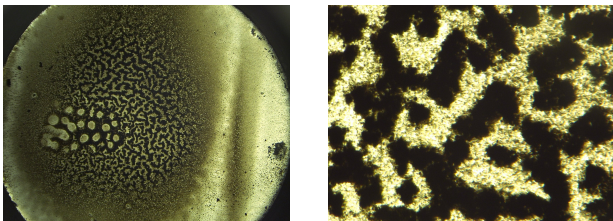
⁹ $\theta \approx \arctan \left| \frac{\vec{V}_{E-field}}{\vec{V}_{flow}} \right|$.

The errors in the analysis technique and ESP collection give some idea as to why there are large deviations between the predicted and experimental results in Fig. 5b.

2.1.3 Optical regime

Due to the very high particle concentrations achieved by the miniCAST aerosol generator, ‘overloaded’ samples were taken by removing air diluters. Several layers of particles could theoretically be deposited over the pin surface in a relatively short time. A 30 minute exposure led to a build up of carbon particles with a thickness of the order of microns; these samples could potentially be analysed using an ATR instrument to obtain absorption spectra. The macroscopic deposition patterns were investigated further, along with the validity of using these samples for ATR analysis.

One overloaded sample was rotated 90° half way during collection, to obtain a more isotropic pattern. Fig. 6 shows the acquired sample. The sample is relatively isotropic about the pin axis. Circular arcing points are also visible¹⁰. Fig. 6b clearly shows an inhomogeneous, counter-intuitive deposition pattern. These patterns were found to be repeatable in the central regions of other overloaded samples.



(a) Full pin image. (b) 1000× magnified image of central pattern.

Figure 6: Overexposed black carbon sample.

Fig. 6a gives further evidence for the claim of inhomogeneous pin collection made in § 2.1.2. Higher concentrations of particles are deposited near the centre of the pin and decrease further away, and there are several factors that might contribute to this effect:

- The tungsten needles were sharpened when the instrument was first constructed. Since the needles are cleaned with IPA before each test run their sharpness might have degraded over time, meaning fewer ions would be formed in the corona. Hence only aerosol particles near the centre of the flow would be charged and deposited.

¹⁰Arcing is not common but could have occurred due to the step change in voltage after the pin was rotated, which is explained by the spike in the current as shown in Fig. 2 at $t \approx 1040$ s.

- Due to manufacturing limitations, the point of each needle is not situated exactly at the point of the triangular collection chamber when the housing is assembled. This could mean that the electric field is not spread homogeneously on the pin surface. Particles could have deposited on the needle itself over time, reducing its functionality.
- The aerosol particles gain charge. Due to inter-molecular Coulomb repulsion charged particles might not follow their trajectories as derived from Eq. 3. More so, the triangle shape of the chamber does not exactly match the geometry of the field. Hence it is possible that charged particles near the edges of the aerosol flow could repel each other and adhere to the chamber walls, giving them a surface charge density and distorting the initial electric field lines towards the axis along which flow travels.

The central pattern is also counter-intuitive. The ESP was designed for single particle deposition, not for overexposure. A continued build up of charged carbon particles might lead to random micron scale lumps of particles on the ground plate. As the incoming particles hit the pin at angles to the vertical (as derived from in Eq. 3), deposition might be more likely to occur on top of these lumps, increasing their height and leading to the stark difference between covered and uncovered regions.

2.1.4 Optical image analysis

A function was written in IDL to visually quantify how black carbon is deposited on a 1000× magnification scale. The function distinguishes each pixel by its colour value (on a 0 - 255 greyscale) depending on whether the pixel is classed as ‘black’, ‘white’, or anywhere in between, i.e. ‘grey’.

Fig. 7 is a histogram showing three distinct regions of colour: a distinct peak for the very dark (i.e. black) pixels, a very narrow bin band full of several white pixels and a ‘plateau’ of low pixel numbers in the bins corresponding to grey colour that the black and white regions. The optical microscope is more absorbing in the blue, so the red histogram was used for image analysis.

Images taken of the central regions of different samples followed a similar trend, and the written IDL function plots the pixels located in this plateau in a new colourscale over a greyscale plot of the initial image. This is shown in Fig. 8. This was done so that the gradual change in colour between black and white could be observed in colour,

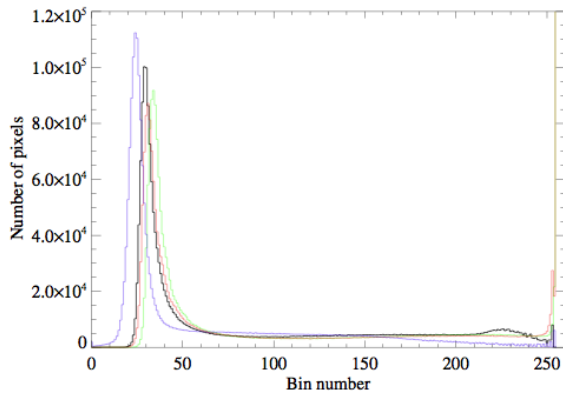


Figure 7: Histogram of Fig. 6b showing pixel distribution according to each pixel's greyscale colour value (0 = black and 255 = white). The red, green and blue curves are histograms for their respective images forming the lossless JPEG-2000 stack. The black curve gives their average.

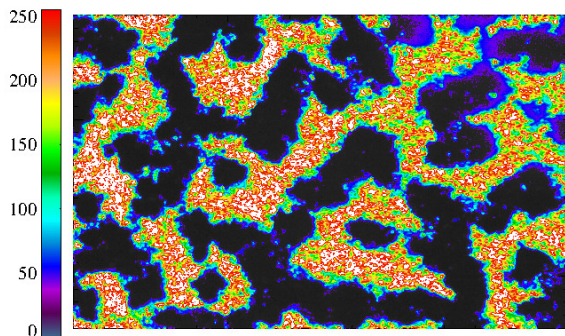


Figure 8: Fig. 6b with overplotted pixel points in the given colourscale, showing how carbon deposition is built up in the 'plateau'.

visualising how carbon is deposited. This method assumes that the pixel colour is linearly related to the number of layers of carbon deposition. This assumption is not entirely correct, but is sufficient for our purposes.

The fraction of area covered by 'black' pixels was also calculated by the function, and this gave a better idea of whether or not the centre of the pin could be feasibly analysed using an ATR instrument. Fig. 6b had a coverage of 43.4%, and similar coverages between 40 - 50% were calculated for other images of the central pattern.

It should be noted that this type of analysis is not feasible for when the ESP is used to sample atmospheric aerosol from a UAV. The atmospheric concentrations are so low that the required exposure times would be much longer than the flight time permits.

2.1.5 ATR spectra

Another important property of aerosols is their absorbance of electromagnetic radiation, and one method of characterising the absorption spectrum of a sample is to use an ATR instrument.

ATR spectroscopy involves measuring changes in an infrared input beam that is totally internally re-

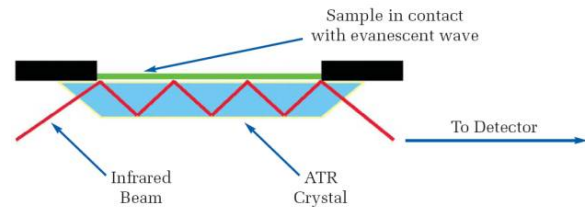


Figure 9: ATR spectroscopy diagrammatic theory of operation [15].

flected through a crystal of refractive index higher than the sample under study (see Fig. 9) [16]. At the boundary between sample and crystal, an evanescent wave propagates of the order $\sim 1\mu\text{m}$ through the sample. The attenuation of this evanescent wave is measured by the reflected beam. A spectrum is formed by varying the input beam wavelength. Each sample will have its own spectrum that gives an idea of its absorption spectrum. Samples similar to Fig. 6 were analysed with a BRUKER ATR spectrometer [17]. Their spectra are shown in Fig. 10.

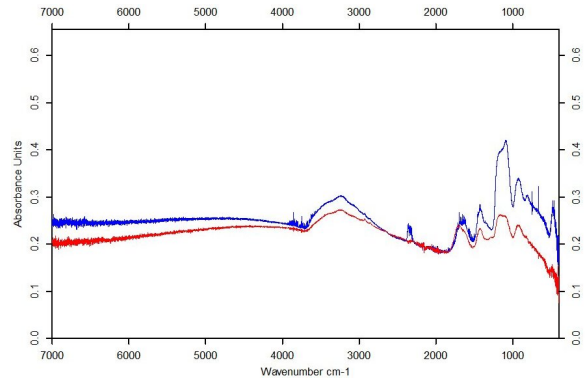


Figure 10: ATR spectra of two overloaded black carbon samples.

Clearly there are reproducible absorption peaks visible at higher wavelengths. This process is highly non-linear, and since the overexposed deposition pattern of black carbon is not uniform and coverage is below 50%, there will be uncertainty in what results are attained and over what wavelength ranges they are valid. The viability of this method is questionable with the current overloaded soot samples that are being collected.

2.2 Sea salt aerosol

The ESP was obtained from RAL and a sea salt aerosol generator was used to test its functionality. The OMRON Nebuliser [18] is designed for medical usage, but its repeatability in the properties of nebulised aerosol led to the instrument being used to generate laboratory sea salt aerosol, as described by Irshad [19]. The purpose of testing the instrument with sea salt aerosols was twofold:

- To better quantify any similarities and differences between overexposed samples of black carbon and sea salt. This would provide information on whether the deposition pattern

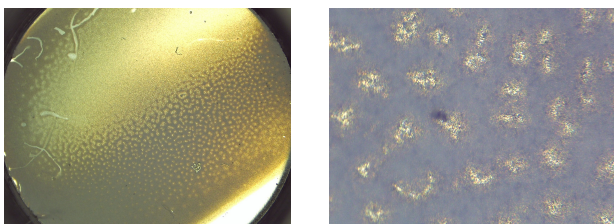
observed in black carbon samples is an intrinsic property of the ESP or due to the aerosol itself.

- To validate ESP operation after transportation from RAL, and to understand how it is controlled with the Arduino boards.

Several experiments were performed with the aerosol to create samples for optical analysis.

2.2.1 Optical image analysis

A similar analysis used in the black carbon investigation was performed on sea salt samples. Fig. 12 shows a very different distribution, however the $1000\times$ magnified pattern established is much more uniform than in the black carbon case. Fig. 11b was 88.8% covered and is a better candidate to result in more valid ATR spectra.



(a) Full pin image. (b) $1000\times$ magnified image of central pattern.

Figure 11: Overexposed sea salt sample.

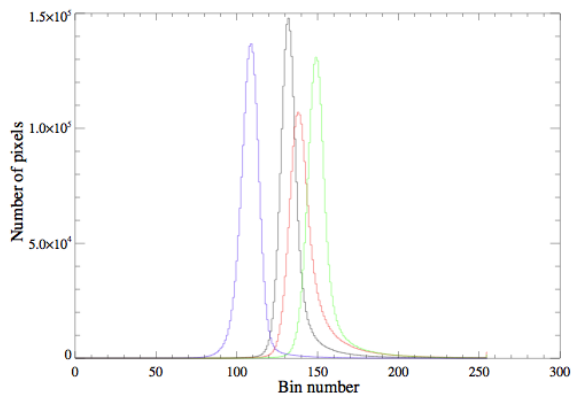


Figure 12: Histogram of Fig. 11b) showing the greyscale pixel colour distribution, in the same style as Fig. 7.

During the collection of a salt sample using one of the three available electrostatic precipitators, deposition was observed on pins linked to the precipitators that were kept off throughout the experiment. This meant that contamination, i.e. diffusion of salt particles onto the pin surface was observed. Even though this deposition is less than the sample collected via electrostatic precipitation, this affects how the instrument is used. It was designed such that three independent samples could be acquired in one test, but clearly this is not the case. With regards to SEM analysis, diffusion of particles to the pin surface could be size dependent, hence the distribution on the pin might not be representative of the aerosol field. The magni-

tude of these contamination effects should be considered further before thinking of re-design ideas.

3 ESP installation in the UAV

After verifying that results can be obtained from ESP samples, we need to consider how this instrument will be used to acquire samples from a real aerosol cloud. Installing the instrument in a UAV needs to be implemented such that it can provide useful data outside of laboratory testing.

3.1 Aerosol inlet design

Having an instrument that effectively samples aerosol is not the only consideration when installing this instrument in a UAV. The path which the aerosol takes from the atmosphere to the collection chamber must also be designed to minimise particle losses and obtain a representative aerosol input¹¹ from which we can sample particles. This section describes the theory behind how the UAV aerosol inlet could be designed and constructed.

3.1.1 Isokinetic sampling

The UAV flies through the atmosphere at an average velocity of 40 mph and hence samples air moving at this velocity¹². We can assume that the flow in front of the UAV is time independent with uniform streamlines that distort around the region of the payload.

Since aerosol particles have an increased mass and inertia compared with air, their trajectories may not follow the streamlines of the fluid flow, especially if these streamlines are subject to sharp changes in direction.

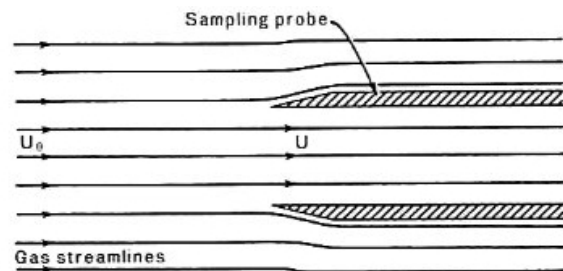


Figure 13: Shape of streamlines from air sample (velocity \vec{U}) to inlet (velocity \vec{U}_0), when velocities are matched in the isokinetic case, hence minimising particle losses at the inlet entry.

Assuming the inlet is placed in a uniform flow, streamlines will distort depending on the velocity of air drawn through with the diaphragm pump. If these velocities are matched, then sampling is isokinetic and streamline distortion is minimal.

¹¹i.e. maintaining the aerosol size distribution properties so that they are not affected between atmosphere and collection.

¹²We can neglect wind speeds, which are much less than 40 mph.

Fig. 13 shows the best case scenario for isokinetic sampling of moving air (i.e. $U=U_0$). If the ESP is to operate at optimal efficiency using a 55 cc min^{-1} flow rate [7], the incoming fluid velocity needs to increase to 40 mph, and this is done by reducing the inlet diameter to 0.45 mm. This diameter is much larger than the size of the aerosol particles that we are concerned with, although blockage by atmospheric debris and water needs to be considered before an inlet this small can be used viably.

3.1.2 Transmission losses

Aerosol particles will be subject to stochastic forces and hence they could diffuse between streamlines. During the aerosol's path between atmosphere and ESP, the loss from particles adhering to the walls of the inlet tube via diffusion is significant and needs to be considered. The settling loss in a circular tube of diameter D_s is given by [11]:

$$\text{Loss} = \frac{2}{\pi} \left(2k_1 k_2 - k_1^{1/3} k_2 + \arcsin \left(k_1^{1/3} \right) \right), \quad (4)$$

$$k_1 = \frac{3LV_T S}{4D_s U}, \quad k_2 = \left(1 - k_1^{2/3} \right)^{1/2},$$

where L is the tube length, $V_T S$ is the settling terminal velocity and U is the flow velocity. Since the inlet to the ESP will be situated facing orthogonal to the UAV velocity direction, a 90° bend will have to be incorporated into the tubing, resulting in further losses:

$$\text{Bend loss} = \left(\frac{\tau U}{D_s} \right) \times \phi \equiv \text{Stk} \times \phi \quad \left(\phi = \frac{\pi}{2} \right), \quad (5)$$

where τ denotes the relaxation time of a particle due to drag effects, ϕ is the bend angle (in radians) and Stk is the Stokes number, which defines how closely suspended particles follow streamlines. Due to the time limitations of this project, transmission losses were not considered for high Reynolds number flow, and the numerical calculations of Stk and fractional loss should be done as further work. If the loss is too high because of the small diameter, then different sized particles will be affected by settling differently. Hence the size distribution will be disrupted and concentration could be severely attenuated, resulting in large experimental deviation from the atmospheric aerosol distribution.

3.1.3 UAV flow distortion

The Reynolds number of the UAV payload can be approximated by assuming a 30 cm diameter sphere moving through air at standard temperature and pressure at 40 mph, giving $\text{Re} \sim O(10^5)$. This flow is clearly turbulent, and this will affect the flow in front of the UAV, which slows down

as explained by Bernoulli's Theorem [20]; the stagnation point at the very front of the payload will have the highest pressure in the flow field. The inlet should protrude from the payload enough such that we sample aerosol whose streamlines have not been distorted by the UAV.

Hoffmann [21] has constructed a finite element method of computing the velocity field around a sphere of Reynolds number 10^4 (forward flow at $\text{Re} \sim 10^4$ will be similar to $\text{Re} \sim 10^5$). By dynamical similarity arguments the distance in front of the sphere where the velocity is similar to what is expected by taking the limit $r \rightarrow \infty$ can be approximated. Fig. 14 shows that when a distance in

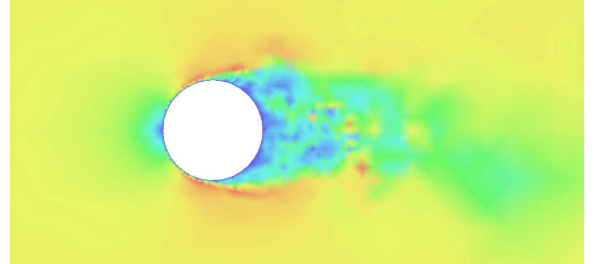


Figure 14: Finite element analysis by Hoffmann [21] of $\text{Re} \sim 10^4$ flow past a sphere. The flow moves from left to right.

front of the sphere is similar to the sphere's diameter, the flow speed ≈ 40 mph. A streamlined elliptically shaped payload as found in the Quest UAV will result in uniform speeds nearer the front stagnation point. If the inlet protrudes a distance at least the length of the payload, then unperturbed air should be sampled.

3.1.4 Prototype inlet

Stainless steel hollow tubing of 0.4 mm inner diameter was sourced and glued to some flexible Polyvinyl chloride tubing so that it could form an airtight link with the ESP. This inlet is by no means viable for atmospheric sampling; it is a preliminary idea that needs to be developed. We need to consider how the inlet fluctuates as the UAV flies with high velocities. In flight vibrations could lead to anisokinetic sampling and further losses.

3.2 Remote control

Currently, the ESP is controlled with Arduino boards and code written specifically for this instrument. There is no method of commanding the ESP to initiate a test without further human input. The code has to be activated remotely with the use of technology available on-board the UAV.

3.2.1 Servos

UAVs, and more generally remote controlled airplanes, use servos to mechanically control the dynamic parts of an aircraft. This includes the ailerons, motor, rudder and elevators. The ground

based transmitter sends PWM¹³ signals that determine the angle at which the elevator is positioned, or the angular frequency of the motor. A servo was acquired from Maplin Electronics [22] and its was used to improve a previously written code [5]. This code can now activate the main operating code once a PWM threshold value has been reached.

4 Further work

This project contributed to an ongoing endeavour. Dr. Peters and his colleagues at RAL have put forward a proposal (based partly on the findings in this project) to further the development of the ESP so that it can be used in a UAV to collect useful samples for analysis. As a result, several ideas were proposed for further studies and testing regarding the realisation of a UAV based *in situ* aerosol particle sampler.

4.1 Re-design

The ESP Housing is robust and easy to clean, but the continuous disassembly and reassembly of the collection chamber between tests will degrade the screws and polycarbonate structures used, potentially leading to fracturing.

As described in §2.1.3, the sharpness of the tungsten needle degrades over several uses, leading to inefficient collection. The needle is also not placed in exactly the correct position, and on these small scales a small deviation would lead to a large error in the expected operation. Both the needle and its housing slot could be developed further.

Scratches and deposition by insertion and removal of the sampling pins from the collection chamber are visible in Fig. 11a and this reduces the pin area that could be analysed. The pin housing needs to be re-designed so that pins are not scratched when handled.

4.1.1 In-flight considerations

Maintaining the ESP instrument for multiple uses within a UAV requires further thought than for laboratory testing.

The probability of a crash landing and the instrument components fracturing or dislodging needs to be considered.

The lower pressure and temperatures of the troposphere at higher altitudes will have an effect on the flow rates and electrostatic precipitation, as well as the Corona discharge and probability of arcing. The PID loop parameters will require adjustments due to the changes in air properties.

¹³Pulse Width Modulation - a method for converting a digital input to an analogue output, by varying the properties of a square wave signal such as the time width of each pulse.

The effect of moisture in aerosol samples is unknown and its effect could be damaging to the components of the instrument or result in a higher probability of arcing.

Exposure times for samples with $\sim 1\%$ loading should be calculated using the Harwell Campus PM 2.5 data¹⁴, assuming the distribution follows Eq. 1. Acquiring optimum samples for analysis will involve trial and error using several exposure times flying at various altitudes and in various weather conditions. After achieving this, the main operating code should be modified to run independently of human input for the duration of the flight. The remote activation code should be adjusted to the specifications of UAV servos that might generate different PWM signals to the test servo.

4.2 Further testing ideas

Vaccum and heat chambers can be used to model upper tropospheric conditions. Wet aerosols can be used to further characterise the ESP's response to moisture. The use of a vibration chamber can simulate in-flight ESP operation. The prototype inlet could be clad with rigid plastic materials to reduce vibrations during flight, and could be tested by analysing samples taken with the inlet installed in the UAV. Due to the high Reynolds number of the inlet ($Re \approx 550$), diffusion losses might be so high that the aerosol sample is heavily attenuated¹⁵. A compromised solution could be to use an inlet with larger diameter that samples air near the stagnant point at the front of the payload that has a lower velocity. These effects on the aerosol distribution should be investigated.

The ESP will hopefully be powered from the same Lithium Polymer battery that supplies power for UAV flight. Hence the battery needs to meet the requirements of the Arduino boards. Testing needs to be done at RAL to validate that the output ESP voltage and current load are similar for a battery power supply compared with what is observed with a computer-powered USB supply.

5 Conclusion

The validity of analysis techniques on ESP aerosol samples was scrutinised. On single particle deposition scales, the experimental size distribution did not match SMPS predictions. There are several reasons behind this discrepancy, including the high voltage needle sharpness and positioning, the fact that sampling of images is not representa-

¹⁴Particulate matter data of the concentration of aerosols with particle diameter $\leq 2.5 \mu m$.

¹⁵Atmospheric aerosols usually have low concentrations, so this is not desirable.

tive of the particle distribution and the limited resolution of SEM imaging. These reasons and others should be considered before the collection chamber is potentially redesigned.

On an optical scale the homogeneity of deposition from two types of aerosol was quantified and the feasibility of using an ATR instrument for analysis of samples was examined. Macroscopic deposition patterns of aerosol particles greatly depend on what aerosol is being deposited, i.e. the intrinsic properties of each compound in question. Hence for general use the ATR is not a technique that would give us significantly repeatable results.

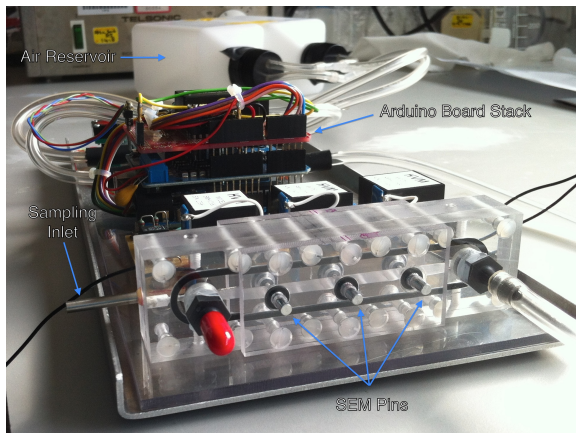
Significant steps were taken towards installing the ESP in a UAV. Code was written to activate the ESP remotely with the aid of an on-board servo. The design of an atmospheric aerosol sampling inlet was theorised before a prototype was manufactured. Due to the open-ended nature of this investigation, there are a broad range of studies that could be carried out as further research.

References

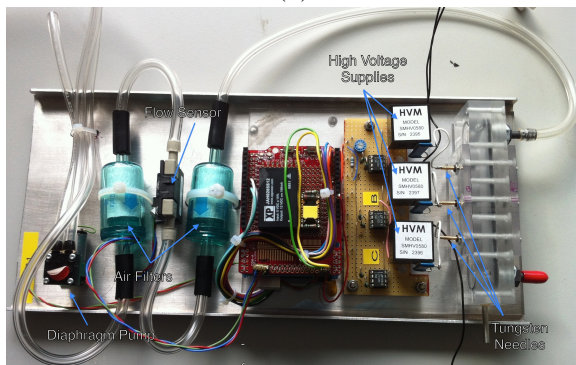
- [1] Spyros N. Pandis John H. Seinfeld. *Atmospheric Chemistry and Physics: From Air Pollution to Climate Change*. Wiley, 2nd edition, 2006.
- [2] Intergovernmental Panel on Climate Change (IPCC). *Climate Change 2013: The Physical Science Basis*. Cambridge University Press, 2013.
- [3] R. J. Griffin. The sources and impacts of tropospheric particulate matter. *Nature Education Knowledge*, 2013.
- [4] Yoram J. Kaufman Yinon Rudich Ilan Koren, Lorraine A. Remer. On the twilight zone between clouds and aerosols. *Geophysical Research Letters*, 2007.
- [5] Kieran Hunt. Instrument to sample and return airborne particles in a volcanic plume. (mphys project). 2013.
- [6] T.T. Morrow, P.E. Mercer. A point to plane electrostatic precipitator for particle size sampling. *American Industrial Hygiene Association*. 25, 8-24, 1964.
- [7] A. Miller. A handheld electrostatic precipitator for sampling airborne particles and nanoparticles. *Aerosol Science and Technology*, 2010.
- [8] R. A. Aplin, K. L. McPheat. Absorption of infra-red radiation by atmospheric molecular cluster-ions. *Atmospheric and Solar-Terrestrial Physics*, 2005.
- [9] Arduino: available at - <http://www.arduino.cc/>.
- [10] Quest uav 300: available at - <http://questuav.co.uk/quest300.php>.
- [11] William C. Hinds. *Aerosol Technology - properties, behavior, and measurement of airborne particles*. Wiley-Interscience, 1999.
- [12] miniCAST. *Real Soot Generator Model 5201 Type A - Instruction Manual*. Jing AG, Switzerland.
- [13] Scanning mobility particle sizer (smps + c): manual available at - <http://www.grimm-aerosol.com/>.
- [14] Imagej software: available at - <http://rsb.info.nih.gov/ij/>.
- [15] Atr: available at - http://las.perkinelmer.com/content/TechnicalInfo/TCH_FTIRATR.pdf, .
- [16] Atr theory: available at - <http://www.piketech.com/files/pdfs/ATRAN611.pdf>, .
- [17] Bruker optics - available at: www.bruker.com/, n.d.
- [18] Omron u-17 ultrasonic nebuliser: available at - <http://www.omron-healthcare.com/eu/en/our-products/respiratory-therapy/ultraair-u17>, 2010.
- [19] R. Irshad. *Laboratory measurements of Sea Salt Aerosol Refractive Index*. PhD thesis, 2009.
- [20] D.J. Tritton. *Physical Fluid Dynamics*. Clarendon Press, 2nd edition, 1988.
- [21] Johan Hoffmann. Adaptive simulation of the sub-critical flow past a sphere.
- [22] Maplin electronics: available at - <http://www.maplin.co.uk/product/servo-and-controller-board-kit-n10jg>.
- [23] Hvm technologies: available at - <http://hvmtech.com/pdf/SMHVSPECsheet.pdf>.
- [24] Honeywell sensing: available at - http://sensing.honeywell.com/product%20page?pr_id=25734.

Acknowledgements

I would like to personally extend my gratitude to Drs. Don Grainger, Adam Povey and Daniel Peters, without whom this project would not have been successful. I am also incredibly grateful to Paul Pattinson for his help with SEM operation, Bob Watkins for his support with pin polishing, and Andy Clack and Jon Temple for their constant help.



(a)



(b)

Figure 15: The ESP instrument, annotated with components.

A The ESP instrument

The high voltage is generated using HVM Tech SMHV0580 regulated high voltage DC to DC converters [23]. The flow rate is measured using a Honeywell AWM3100V hot wire mass flow sensor [24]. Filters were placed either side of the MFM sensor to reduce its degradation due to incoming aerosol particles. The flow through the instrument (being generated with the diaphragm pump) displays periodic oscillations that could diverge if left to run without damping, hence two 0.5 L bottles that acted as an air reservoir were connected in parallel between the pump and mass flow meter. This allowed the reservoir to stabilise the flow fluctuations and incorporate a measurable timescale to the oscillations.

The UAV payload also has dimensions $12\text{ cm} \times 12.5\text{ cm} \times 16\text{ cm}$ into which the whole instrument must fit.

The stack of Arduino boards has the following responsibilities:

- Top - Mass flow meter and power converter from 5 to 12 V. A PWM DAC board also interconnects to the EHT board.
- Middle - motor shield board that runs the pump.
- Bottom - Arduino UNO board through which

commands are echoed and operating variables are changed.

The EHT board includes the 3 HVM high voltage power supplies and 3 special op-amps configured as MUX switch and gain to change a 3.3V DAC signal to a 5V DAC signal that controls the EHT supplies.

B Sea salt aerosol experiments

Fig. 16 shows the experimental setup of how sea salt aerosol was nebulised from a 3.1% solution, dried and sampled with the ESP. A routine was established in order to provide repeatable aerosols and useful samples.

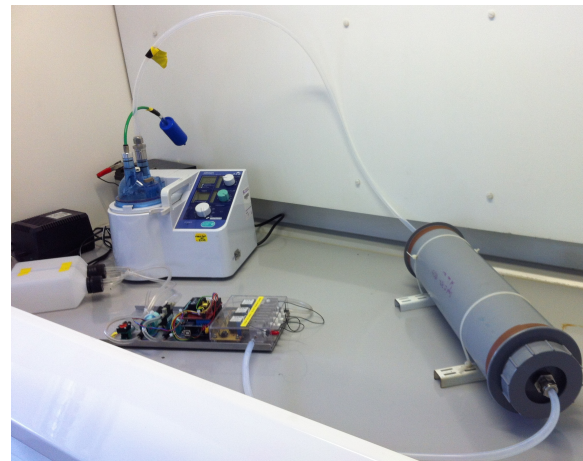


Figure 16: Experimental setup connecting the OMRON Nebuliser to a diffusion dryer that removes moisture before the ESP samples the aerosol.

- The nebuliser was turned on 20 minutes before the ESP, to allow the ultrasonic aerosol generation process to stabilise.
- The nebuliser was set up with a flow rate of 1 and nebulisation rate 10. After the nebulised suspension passed through a diffusion dryer to remove all moisture¹⁶, an aerosol distribution with properties of $1.52\mu\text{m}$ mean diameter and concentration $\approx 3.37 \times 10^6\text{ cc}^{-1}$ [19]. From these properties one could estimate the exposure times required to completely cover the pin head in several layers of sea salt particles.
- The total volume of enclosed air in the system was calculated, as well as the time required for the system to be purged of non-filtered air. The ESP diaphragm pump was switched on with a 55cc/min flow rate for at least 35 minutes to completely purge the system.
- The ESP voltage was switched on and testing began.
- After testing, the ESP was shut down. The

¹⁶Moisture might result in increased probability of arcing, and could deposit aerosols further down the tubing which is not desirable.

pin samples were removed quickly¹⁷ and imaged. The instrument was then left for at least 12 hours for the voltage to dissipate.

¹⁷Salt samples degrade with time due to collection of moisture from the atmosphere.

C Arduino remote activation code

```

#include <Average.h>
int servoIn = 0; //digital pin 2 corresponds to interrupt 0//
float t= 0; //length of peak in ms//
volatile int i = 0; //counter//
volatile int j = 0; //counter//
volatile int counterarray[50];
volatile int timediff[50];
int x[25];
int ratiovalue;
int waiting = true;
volatile unsigned long timearray[50];
int threshold = 24; //PWM threshold value//

void setup(){//interrupt subroutine marks time when PWM signal changes value//
  Serial.begin(9600);
  attachInterrupt(servoIn , PWMread, CHANGE);
  Serial.println("START");
  delay(1000);
}

void PWMread(){
  counterarray[i] = i;
  timearray[i] = micros();
  i++;
  if(i == 50){
    i=0;
  }
}

void loop(){
  while(waiting){
    delay(1000);
    Serial.println("CLEAR");
    delay(1000);

    for(j=2; j<=47; j++){
      Serial.print(' ');
      Serial.print(counterarray[j]);
      Serial.print(' ');
      timediff[j] = timearray[j+1]-timearray[j];
      Serial.print(' ');
      Serial.print(timediff[j]);

      if(j%2){
    }
      else{
        if(timediff[j+1] > timediff[j]){
          ratio[j]=(timediff[j+1])/(timediff[j]);
        }
        else{
          ratio[j]=(timediff[j])/(timediff[j+1]);
        }
      }
      Serial.print(" ratios");
      Serial.print(counterarray[j]);
      Serial.print(' ');
      Serial.println(ratio[j]);
      x[j] = ratio[j];
    }
  }
}

```

```
    }
    delay(1000);
    ratiovalue = mode(x,25);
    Serial.print(" ratiovalue ");
    Serial.println(ratiovalue);
    delay(1000);
    if(ratiovalue >= threshold){
        waiting = false;
    }
}
if(!waiting){
    //Initiate main code//
}
}
```